1   # *Switch-like control of helicase processivity by single-stranded DNA*

2   # *binding protein*

3

4   **Barbara Stekas[1], Masayoshi Honda[2], Maria Spies[2], Yann R. Chemla[1,3,*]**

5   *[1]Department of Physics, University of Illinois, Urbana-Champaign, Urbana*

6   *[2]Department of Biochemistry, Carver College of Medicine, University of Iowa, Iowa City*

7   *[3]Center for the Physics of Living Cells, University of Illinois, Urbana-Champaign, Urbana*

8

9   Helicases utilize the energy of NTP hydrolysis to translocate along single-stranded nucleic acids (NA) and

10   unwind the duplex. In the cell, helicases function in the context of other NA-associated proteins which

11   regulate helicase function. For example, single-stranded DNA binding proteins are known to enhance

12   helicase activity, although the underlying mechanisms remain largely unknown. *F. acidarmanus* XPD

13   helicase serves as a model for understanding the molecular mechanisms of Superfamily 2B helicases, and

14   previous work has shown that its activity is enhanced by the cognate single-stranded DNA binding protein

15   RPA2. Here, single-molecule optical trap measurements of the unwinding activity of a single XPD helicase

16   in the presence of RPA2 reveal a mechanism in which XPD interconverts between two states with different

17   processivities and transient RPA2 interactions stabilize the more processive state, activating a latent

18   "processivity switch" in XPD. These findings provide new insights on mechanisms of helicase regulation

19   by accessory proteins.

20

21   *For correspondence: ychemla@illinois.edu

Introduction

2   Helicases are molecular machines that use the energy of NTP hydrolysis to separate the strands of

3   nucleic acid (NA) duplexes. A large class of helicases unwind by translocating directionally along a single

4   NA strand and can utilize this translocation activity to displace NA-bound proteins (1-4). In the cell,

5   helicases are involved in many essential genome maintenance processes, including replication,

6   recombination, and repair (5-7). In a number of instances, the same helicase is known to carry out several

7   of these disparate functions (4,8,9). Thus, helicase activity must be tightly regulated, not only to prevent

8   indiscriminate unwinding of duplex DNA in the cell, which could lead to genome instability, but also to

9   define the context-dependent role of the helicase. How this regulation occurs is often unclear, but

10   growing evidence points to interactions with protein partners as one regulatory mechanism (4,8,9).

11   Xeroderma pigmentosum group D (XPD) protein is a 5' to 3' DNA helicase that serves as a model for

12   understanding members of the structural Superfamily 2B (SF2B) of helicases, a group that includes yeast

13   Rad3 and human FANCJ, RTEL, and CHLR1 (9-12). Human XPD is part of transcription factor IIH (TFIIH) and

14   plays a vital role in nucleotide excision repair (NER) (13-16). It has also been shown to participate in

15   chromosome segregation (17) and in the cell's defense against retroviral infection (18). Structurally, XPD

16   consists of a conserved motor core (**Fig. 1a**)—helicase domains 1 and 2 (HD1 and HD2)—that couples ATP

17   binding and hydrolysis to translocation on ssDNA, a FeS cluster-containing domain, and a unique ARCH

18   domain that encircles the translocating strand (19-23).

19   As it functions on ssDNA, XPD is expected to encounter other proteins such as Replication protein A

20   (RPA), which binds single-stranded DNA non-sequence specifically. Single-stranded DNA binding proteins

21   function as protectors of ssDNA against nucleolytic damage and play important regulatory roles (24). Due

22   to their ubiquity, frequent interactions with other DNA-bound proteins are likely (25). Single-stranded

23   binding proteins are known to stimulate the DNA unwinding activity of SF2 helicases, although the

24   mechanisms of enhancement remain elusive (26-31). In the present work, we investigate the effect of

25   single-stranded DNA binding proteins on helicase unwinding activity using XPD from *Ferroplasma*

26   *acidarmanus* as a model system due to the availability of biochemical (31) and single-molecule kinetic

27   data (32-34), as well as structural information from homologs (20-22,35). Prior work (31) has shown that

28   *Fac*XPD unwinding is enhanced greatly by one type of cognate ssDNA-binding protein in *F. acidarmanus*,

29   RPA2, more so than a second cognate protein, RPA1, or by heterologous proteins. *Fac*RPA2 has a simple,

30   single-domain architecture with one OB fold that occludes ~4 nt of ssDNA (**Fig. 1b**) (31). Single-molecule

31   experiments demonstrated that XPD can occupy the same DNA strand as RPA2 and bypass RPA2-bound

1   ssDNA (32). Crucially, no direct, specific interactions between RPA2 and XPD in solution have been

2   observed (31).

3   How an ssDNA-binding protein with no known protein-protein contacts to the helicase stimulates

4   helicase-mediated DNA unwinding activity remains an open question, and makes *Fac*XPD and *Fac*RPA2 an

5   intriguing system for studying the stimulatory effects of ssDNA-binding proteins on helicases. Mechanisms

6   for enhancement of unwinding activity can loosely be placed in three categories (31). First, an ssDNA-

7   binding protein could destabilize the DNA duplex at the ssDNA-dsDNA junction ahead of the helicase,

8   facilitating its motion forward. Second, it could enhance unwinding by sequestering ssDNA and providing

9   a physical barrier to helicase backsliding, i.e. rectifying helicase forward motion. Lastly, it could activate

10   the helicase for processive unwinding through direct interactions with the helicase-DNA complex.

11   Here, we use a single-molecule optical trap assay to observe individual proteins of XPD unwinding

12   DNA and to analyze the effects of RPA2 on their unwinding activity. While previous reports have shown

13   that RPA2 is able to enhance XPD activity (31,32), they have not defined what aspects of activity is

14   enhanced or provided a mechanism. Our results show that RPA2 primarily increases XPD processivity, or

15   the maximum number of base pairs unwound. XPD exhibits repeated attempts to unwind duplex DNA and

16   RPA2 increases the frequency of attempts that have high processivity. While RPA2 can transiently

17   destabilize duplex DNA, this does not promote XPD unwinding. Instead, data point to a mechanism in

18   which XPD possesses a latent processivity "switch" which is activated by RPA2. Our measurements shed

19   new light on the mechanisms by which accessory proteins such as single-stranded DNA binding proteins

20   can enhance helicase activity.

21

Results

23   **XPD processivity increases in the presence of RPA2**

24   As shown in **Fig. 1c**, we monitored the activity of a single XPD in the absence and presence of RPA2 in

25   solution from the unwinding of an 89-bp DNA hairpin (**Figure 1—Figure Supplement 1**) tethered between

26   two optically trapped beads and stretched under constant force (12 pN), as described previously (33).

27   Data were collected at a rate of 89 Hz. Unwinding of the hairpin was detected from the increase in the

28   end-to-end extension of the DNA tether, as each broken base pair released 2 nucleotides (see **Methods**).

29   An abasic site positioned at the 3' end of the hairpin prevented XPD from unwinding the long (1.5-kb)

30   dsDNA handle used to separate the hairpin from the trapped beads (33) (**Figure 1—Figure Supplement**

31   **1**). To control the loading of XPD and RPA2 onto the hairpin, we used a custom flow chamber consisting

1   of parallel laminar-flow streams containing different buffers, as described previously (36) (see **Methods**;

2   **Figure 1—Figure Supplement 2**). Placing the hairpin in one stream containing XPD but no ATP for ~1 min.,

3   the protein was allowed to bind to a 10-dT ssDNA loading site—approximately equal to the footprint of a

4   single XPD (33,37)—at the 5' end of the hairpin (**Figure 1—Figure Supplement 1**). Unwinding was initiated

5   by moving the hairpin to a stream containing saturating ATP (500 µM) and varying concentrations of RPA2

6   (0-50 nM). This procedure ensured that a single XPD was loaded at one time, and that the unwinding

7   observed resulted from that of a single XPD helicase in the absence or presence of many RPA2 molecules

8   in solution (see **Methods**).

9   **Figure 1d** shows representative traces of a single XPD protein unwinding in increasing [RPA2]. As

10   previously reported, XPD unwound in repeated "bursts," comprising cycles of forward unwinding motion

11   followed by backward rezipping (33), repeating a number of times (5 ± 1) until the protein dissociated. In

12   the absence of RPA2, we observe that the processivity—the maximum hairpin position reached by XPD

13   during any one burst—was low, on average 15-20 out of 89 bp, consistent with our prior work (33). With

14   increasing [RPA2], XPD unwound farther into the hairpin, occasionally unwinding the entire 89-bp hairpin

15   stem (e.g. t = 20 s for 5 nM RPA2 or t = 30 s, 70 s for 50 nM RPA2 in **Fig. 1d**).

16   Each burst represents an attempt by one XPD molecule to unwind the hairpin, and we found that

17   processivity varied greatly from burst to burst. Each burst consisted of varying extents of duplex

18   unwinding followed by rezipping, often to the base of the hairpin. As shown in the representative trace in

19   **Fig. 2a**, several molecular events comprised backward motion: XPD backstepping or backsliding via

20   temporary disengagement from the unwinding DNA strand (**Fig. 2b**: diagram 1a and 1b), or translocation

21   on the other hairpin strand away from the fork junction (2 and 3), all leading to DNA rezipping under its

22   regression force. An example of the latter occurred when XPD completely unwound the hairpin stem and

23   translocated past the dT tetraloop cap onto the opposing strand, allowing the stem to rezip gradually in

24   the protein's wake (**Fig. 2b**: diagram 2). In a contrasting example, we observed gradual rezipping of the

25   duplex mid-hairpin, which we attributed to XPD disengaging from its DNA strand to switch to the opposing

26   strand (**Fig. 2b**: diagram 3), a behavior reported for other helicases (38,39). This interpretation is

27   corroborated by the observation that gradual rezipping was typically followed by a stall at ~10 bp (**Fig. 2a**,

28   t = 58 s) the size of XPD's footprint, consistent with the protein stalling at the abasic site on the 3' strand

29   at the base of the hairpin. Subsequent unwinding bursts were presumably due to XPD strand-switching

30   back to the original strand. In contrast, rapid rezipping events due to backsliding usually occurred to the

31   base of the hairpin (**Fig. 2a**, t = 44 s), consistent with the protein remaining on the hairpin 5' strand.

4

1   We analyzed the processivity of each burst as a function of [RPA2], as shown in the scatter plot in **Fig.**

2   **2c**. In the absence of RPA2, nearly all the individual burst processivities cluster below 25 bp, with a small

3   fraction (<10%) extending further. When unwinding in the presence of RPA2, the average burst

4   processivity increases with [RPA2] up to 35 bp at 50 nM RPA2. However, the distributions of burst

5   processivity at each RPA2 concentration show a significant fraction at relatively low processivity, ≲25 bp,

6   persisting across all concentrations. As [RPA2] increases, an increasing fraction of bursts fall into a higher

7   processivity tail of the distribution, which includes many cases of complete unwinding of the 89-bp

8   hairpin. The distribution of burst processivity for all [RPA2] (**Fig. 2d**) shows a large population of bursts

9   with average processivity of 15-20 bp, followed by a long tail with processivity extending from 25 to 89

10   bp.

11

12   **Melting of the hairpin by RPA2 does not aid XPD unwinding**

13   We next asked by what mechanism RPA2 increases the processivity of XPD. One possibility is that

14   RPA2 helps destabilize the duplex, assisting XPD in unwinding. In such a duplex melting mechanism (31),

15   RPA2 would presumably bind at the ssDNA-dsDNA junction and melt several base pairs ahead of XPD.

16   Because XPD relies heavily on thermal fluctuations to help it break the base pairing bonds ahead of it (33),

17   RPA2 lowering the energy barrier to unzipping the duplex could plausibly enhance XPD's unwinding

18   activity.

19   As shown in **Fig. 3a**, RPA2 is capable of transiently destabilizing hairpin DNA under force of 12 pN. In

20   experiments with RPA2 but without XPD, short melting events are observed, corresponding to the hairpin

21   opening by ~5-6 bp, comparable to the footprint of RPA2 (31), and reannealing shortly thereafter (~20

22   ms). [Such transient melting is also observed in **Fig. 1d** after XPD dissociation (e.g. at t > 110 s for 50 nM

23   RPA2).] These melting events become more frequent as the concentration of RPA2 is increased (**Figure**

24   **3—Figure Supplement 1**), in support of melting being RPA2-mediated. Analyzing the times between

25   melting events, we estimate an effective second-order rate constant of $(1.2 \pm 0.3) \times 10^8$ M^{-1} s^{-1} for binding.

26   RPA2-mediated melting events are also observable as XPD unwinds in the presence of RPA2 (**Fig. 3b**).

27   Such events are identifiable over XPD unwinding dynamics due to their characteristic size (~5-6 bp) and

28   short lifetime (~20 ms) (**Fig. 3b**, inset; see **Methods** and **Figure 3—Figure Supplement 2**). While some false

29   positives are detected in the absence of RPA2, they are uncommon and the frequency of detected melting

30   events increases with [RPA2] (**Fig. 3c**), confirming their connection to RPA2 activity. This finding indicates

31   that RPA2 is capable of binding at the same fork junction as XPD and melting DNA ahead of the helicase.

32   However the question remains whether RPA2 transient melting aids XPD in unwinding.

5

1 To answer this question, we determined how RPA2-mediated melting events impact the forward
2 progress of the helicase. If duplex destabilization aids in unwinding, we suspected XPD may be more likely
3 to advance along the DNA during melting events. To this end, we examined the position of the helicase
4 on the hairpin prior to each RPA2 melting event and after the duplex reannealed. We identified many (N
5 $\approx$ 400) individual melting events during XPD unwinding and aligned them along the position axis such that
6 each event began at 0 bp before melting occurred (**Fig. 3d**, schematic). We then independently aligned
7 the melting and reannealing transition of each event in time at $t = t_{melt}$ and $t = t_{anneal}$, respectively (**Fig. 3d**,
8 "before" and "after" schematic). As shown in **Figure 3e,** the resulting probability density of these aligned
9 traces reveals the average position of XPD prior to and following an RPA2 melting event (see **Methods**).
10 After a melting event, we find that the hairpin is most likely to reanneal all the way back to the same
11 position as before the event, indicating that XPD has not moved from its initial position. Importantly, this
12 result shows that there is no significant forward movement of XPD as a result of RPA2 duplex melting, and
13 that XPD does not exploit RPA2's melting activity to enhance its own unwinding.

14 **Figure 3f** shows a control in which the alignment process above was repeated at random points during
15 unwinding, each point paired with one $t = 0.06$ s after, corresponding to the time window over which we
16 searched and identified RPA2 melting events (see **Methods**). Again, XPD on average shows no net progress
17 in this amount of time. Comparing **Figure 3e** and **3f** shows that the RPA2-mediated melting events have
18 little to no impact on XPD movement.

19

20 **XPD exhibits two distinct types of activity, the fraction of which depends on RPA2**

21 The burst processivities at different [RPA2] (**Fig. 2c**) show that a persistent and significant fraction of
22 bursts exhibit relatively low processivity, $\lesssim$25 bp. Bursts with higher processivity extending from 25 to 89
23 bp also exist at all [RPA2], with their number apparently increasing as [RPA2] increases. An important
24 question is whether there exist any characteristic differences between bursts during which more or less
25 DNA is unwound.

26 To answer this question, we grouped bursts into two categories: "high-processivity" or "low-
27 processivity" depending on whether or not a threshold of 25 bp was exceeded, this value chosen based
28 on where the tail in the distribution of processivities occurred (**Fig. 2c**). **Figure 4a** shows the unwinding
29 portions of many bursts aligned to begin at the same time ($t = 0$), color coded by [RPA2] and processivity
30 category (light color for low-processivity; dark color for high-processivity; see **Table 1** for number of data
31 traces). When grouped in this manner, some notable features emerge. The fraction of bursts categorized
32 as high processivity increases clearly with RPA2 concentration (**Fig. 4a**) saturating to ~50% at RPA2

1   concentrations >10 nM (**Fig. 4b**). Furthermore, long stalls (sometimes exceeding tens of seconds in

2   duration) around 10-15 bp are evident at all concentrations and in both high- and low-processivity traces.

3   This stalling behavior has been reported previously (33) and attributed to XPD's encounter with GC-rich

4   regions—which are more difficult to unwind due to higher base-pairing energy—at this position in the

5   hairpin. All low-processivity bursts exhibit these stalls, after which XPD either backslides to the base of

6   the hairpin or dissociates, ending the burst. However, we have observed XPD continue unwinding past 25

7   bp after a long stall and be categorized as "high processivity".

8   Importantly, we do not observe significant differences between bursts of the same processivity

9   category obtained at different RPA2 concentrations. **Figure 4c** shows all unwinding bursts for high and

10   low processivity types averaged together at each RPA2 concentration (color coded the same as in **Fig. 4a**)

11   and across all RPA2 concentrations (black and gray lines, respectively). The averaged unwinding traces

12   exhibit the same behavior independent of RPA2 concentration. Low-processivity bursts all display stalls at

13   ~10 bp, whereas high-processivity bursts unwind past this region. Burst-to-burst differences are reflected

14   by the shaded areas and are consistently smaller than the differences between the two processivity

15   categories. This finding is corroborated when analyzing the velocity of XPD. **Figure 4—Figure Supplement**

16   **1** shows the average unwinding velocity determined separately for low- and high-processivity bursts at

17   each RPA2 concentration as a function of XPD's position on the hairpin. While XPD on average slows down

18   near 10 bp due to the high GC content of this section of the hairpin, the velocity of highly-processive bursts

19   is consistently higher than for low-processivity bursts at this position. On the other hand, differences in

20   velocity are insignificant across varying [RPA2] within the same processivity category.

21   We also find that both low- and high-processivity burst durations remain constant with RPA2

22   concentration (**Figure 4—Figure Supplement 2**, gray and open data points, respectively). The more

23   processive bursts tend to have longer durations since XPD travels a longer distance on DNA, and

24   processivity increases with [RPA2]. The increase in burst duration observed when combining both types

25   of bursts is explained simply from the increase in the fraction of high-processivity bursts with increasing

26   [RPA2].

27   Our results show that high-processivity unwinding in the absence of RPA2 is indistinguishable from

28   that in the presence of RPA2 and likewise for low-processivity unwinding. All parameters we quantified

29   by burst in the same processivity category are independent of [RPA2]. Instead [RPA2] increases the

30   probability of high-processivity bursts. These findings suggest that high- and low-processivity unwinding

31   correspond to intrinsic states of XPD, with RPA2 increasing the likelihood of XPD being in its more

32   processive state.

1

Discussion

3   From our results, we propose that XPD can adopt two intrinsic states, one competent for high-

4   processivity unwinding and the other not. Both states are populated independently of RPA2; highly

5   processive unwinding activity can occur in the absence of RPA2 and is indistinguishable from that detected

6   in the presence of RPA2. RPA2 does not assist XPD unwinding by directly destabilizing the duplex, but

7   rather by shifting the equilibrium toward the high-processivity state. In the data we have collected, the

8   two states are effectively hidden, and we can infer their presence only from the processivity exhibited by

9   XPD, i.e. whether XPD unwinds beyond a threshold we have selected as 25 bp.

10   **Figure 5a** shows a simple kinetic scheme that describes this model quantitatively. XPD can alternate

11   between "low" and "high" processivity states with rate constants k_1 and k_{-1}. Here, we assume k_1 to be

12   dependent on RPA2 concentration, whereas all other rate constants are independent of RPA2. In the high

13   processivity state, XPD reaches the 25 bp threshold—and is scored as high processivity—at a rate k_2,

14   corresponding to the time XPD takes to unwind 25 bp, which encompasses all forward and backward steps

15   to this position. Finally, we assume that XPD can dissociate from the DNA in the low processivity state

16   with rate constant k_{off}. Given this kinetic scheme, we derive an expression for the probability, $P_{>25}(t)$, that

17   a given XPD molecule unwinds >25 bp by time t (see **Methods**), which can be compared directly to

18   experimental data (**Fig. 5c**), obtained from the fraction of XPD molecules that have crossed the 25-bp

19   threshold at each time point (**Fig. 5b**).

20   **Figure 5c** shows a global fit to our data using different values of k_1 for each RPA2 concentration but a

21   common set of values of k_{-1}, k_2, and k_{off}. The parameter values can be found in **Table 2**. (We considered

22   an alternative model in which XPD can dissociate in both its low- and high-processivity states by

23   introducing an additional rate constant k'_{off} (see **Methods**). The best fit to the data yielded negligible values

24   for k'_{off}, indicating that XPD dissociation occurs in its low processivity state but is unlikely from its high

25   processivity state.) The value obtained for k_{off} predicts that XPD remains bound to DNA for an average

26   lifetime of 25 s, consistent with observation. A value of $k_2 = 0.17 \pm 0.02$ s^{-1} matches that expected for XPD

27   to unwind 25 bp at an average speed of 4-5 bp/s (33) (**Figure 4—Figure Supplement Fig. 1a**). Finally, we

28   find that k_1 increases linearly with RPA2 concentration (**Fig. 5d**) with a slope of $(1.5 \pm 0.5) \times 10^7$ M^{-1} s^{-1}. The

29   linear dependence on [RPA2] suggests that a simple second-order reaction between RPA2 and the XPD-

30   DNA complex shifts the equilibrium to the high processivity state. The intercept of $1-2 \times 10^{-2}$ s^{-1} provides

31   a basal rate of interconversion between the two processivity states in the absence of RPA2. This simple

1   kinetic model can also be compared to our other results. The fraction of high processivity XPD bursts

2   measured vs. RPA2 (**Fig. 4c**) is well fit by the model with no additional fitting parameters (see **Methods**).

3   Likewise, the average burst duration (**Figure 4—Figure Supplement 2**) is well described by the same model

4   (see **Methods**).

5   Although the success of this kinetic model in fitting the data supports our two-state processivity

6   model, it is agnostic to the underlying mechanism of processivity enhancement. We thus must look to

7   other evidence to identify plausible mechanisms. The dependence of the rate k_1 on RPA2 concentration

8   suggests that RPA2 binding to the XPD-DNA complex may activate it for processive unwinding; the linear

9   dependence on [RPA2] rules out mechanisms in which multiple RPA2 bind cooperatively. RPA2 could be

10   binding to DNA, the protein, or both. We have already explored some mechanisms in which RPA2 binding

11   to DNA enhances XPD activity. Our results in **Figure 3** rule out RPA2 melting of DNA as a plausible

12   mechanism. They also disfavor a sequestration mechanism, in which RPA2 binding to ssDNA behind XPD

13   inhibits retrograde motion. By acting as a physical barrier against XPD back-stepping or back-sliding

14   (**Figure 4—Figure Supplement 2a**), two behaviors often exhibited by XPD during unwinding (33), ssDNA

15   sequestration may enhance processivity. Since each burst involves XPD-mediated DNA unwinding

16   followed by rezipping to the base of the hairpin, the duration of a burst provides information on the

17   amount of back-stepping. Bursts with more back-steps are expected to be shorter in duration and vice

18   versa. However, as shown in **Figure 4—Figure Supplement 2b**, we do not observe the mean duration of

19   either the low or high-processivity bursts to increase with RPA2, as predicted by a sequestration

20   mechanism.

21   Alternately, RPA2 may interact directly with XPD (**Figure 4—Figure Supplement 3**). Direct RPA-

22   helicase interactions have been detected for the Superfamily 2 human helicases WRN, BLM, RECQ, and

23   FANCJ and shown to increase helicase activity (29,30,40-42). While no strong interactions between

24   *Fac*XPD and *Fac*RPA2 have been reported in solution (31), formation of a XPD-RPA2 complex on DNA may

25   be possible. To test such a mechanism, we carried out an experiment in which we allowed a complex of

26   XPD and RPA2 to form on DNA in the absence of ATP, then provided ATP for unwinding. Here, we utilized

27   a different flow chamber configuration in which one stream contained XPD and RPA2 (**Figure 4—Figure**

28   **Supplement 3b**; red stream) but no ATP, and another stream contained ATP but no protein (blue stream).

29   We placed the DNA hairpin in the protein stream for 40-60 s, then moved it into the ATP stream to observe

30   unwinding. If XPD and RPA2 were to form a complex with higher processivity than XPD alone, we would

31   expect more processive activity at higher RPA2 concentrations as the probability of a complex forming

32   should increase. However, we observed no effect on processivity across RPA2 concentration (**Figure 4—**

9

1   **Figure Supplement 3c**); the fraction of bursts that exhibited high processivity (>25 bp) remained constant.

2   The addition of non-hydrolyzable ATP analog ATP-γS to the protein stream had no measureable impact

3   (data not shown). This result indicates that any complex formed would be short-lived, and would not

4   survive the move between the protein and ATP streams, which takes up to ~10 s. The rate constant k_{-1} in

5   our kinetic model (**Fig. 5a**) determines the lifetime of the high-processivity state, and its value obtained

6   from a global fit to the data gives a lifetime of ~8 s, consistent with this interpretation. The transience of

7   the interaction may also explain why an XPD molecule may revert to low processivity activity after a high

8   processivity burst and vice versa.

9   Alternate mechanisms involving transient RPA2 binding to DNA may be more plausible. Recent studies

10 (43) suggest that the displaced (non-translocating) DNA strand may play an inhibitory role for some

11 helicases by binding to secondary sites on the protein surface. Protein binding to the displaced ssDNA

12 could reduce the strand's inhibitory interaction with the helicase, enhancing unwinding activity. XPD is

13 known to possess a secondary binding site for the (3') displaced strand located on the HD1 domain, under

14 the ARCH domain (22,44) (**Fig. 1a**). This site is not only important for DNA fork positioning but also plays

15 a regulatory role, likely acting as a throttle to unwinding. In the homologous *T. aquaticus* XPD, a point

16 mutation disrupting this secondary binding site enhances unwinding and force generation (44). Structural

17 analysis of XPD and homologs maps ~5 nt of ssDNA to this secondary site between the DNA fork at the

18 FeS cluster and the entry tunnel into the motor core (33,37,44). Thus, RPA2 binding of 5 nt of ssDNA would

19 disrupt XPD-ssDNA contacts at this secondary site and could similarly activate XPD unwinding. Moreover,

20 previous single-molecule measurements (33) showed that individual XPD exhibit 5-bp backward/forward

21 step pairs (see also **Figure 3—Figure Supplement 2**; blue box), attributed to the transient

22 release/recapture of 5 nt of ssDNA from the secondary site. In the presence of RPA2, we observe the

23 frequency of such events decrease (**Figure 3—Figure Supplement 2**; compare blue box for 0 nM to 50 nm

24 RPA2), consistent with the idea that RPA2 may affect DNA contacts to this regulatory site.

25   Helicases are likely to encounter other DNA-bound proteins in the cell, and such molecular

26 associations have the potential to regulate helicase activity. Our results provide new insights into the

27 possible mechanisms by which accessory proteins can affect helicases. We show how a single-stranded

28 DNA binding protein can enhance helicase processivity through transient interactions with the helicase-

29 DNA complex which can activate a "processivity switch". We speculate on the latent conformational states

30 that could be controlled by this switch. The evidence above points to alternate DNA binding configurations

31 (33,44) that regulate unwinding activity, but there may be other possibilities. An intriguing example is the

32 ARCH domain of XPD, which has been shown to interconvert dynamically between two conformations

1   (34). However, while these states are connected to DNA damage recognition (34), their roles in unwinding

2   have yet to be defined. The general mechanism described here for XPD may apply broadly to other

3   helicases. Recent studies of SF2 helicase RecQ (43) suggest a similar inhibitory role of a secondary DNA

4   binding site, which could plausibly be modulated by DNA-binding proteins. Likewise, studies on SF1

5   helicases UvrD, Rep, and PcrA have shown that alternate conformations of one subdomain strongly affect

6   activity, particularly processivity (39,45). Interactions with protein partners favoring particular subdomain

7   conformations may provide a mechanism for activating processive unwinding (45,46). Identifying the

8   molecular details of the conformational states that produce high and low processivity activity is a rich

9   subject ripe for future investigation.

10

Acknowledgements

Methods

DNA Construct Synthesis. The hairpin construct was synthesized as described in Qi *et al.* (33). The construct consists of three separate dsDNA fragments ligated together after synthesis and purification (**Figure 1—Figure Supplement 1**): a 1.5-kb 'Right handle', an 89-bp 'Hairpin' stem capped by a $(dT)_4$ loop, and a 1.5-kb 'Left Handle'. 'Right handle' and 'Left handle' are functionalized with a 5' digoxigenin and biotin, respectively, for binding to anti-digoxigenin and streptavidin coated beads. The hairpin stem sequence used for all experiments was identical to 'Sequence 1' used in Ref. (33), which contains a random 49% GC sequence: 5'-GGC TGA TAG CTG AGC GGT CGG TAT TTC AAA AGT CAA CGT ACT GAT CAC GCT GGA TCC TAG AGT CAA CGT ACT GAT CAC GCT GGA TCC TA-3'. The hairpin stem is flanked by a 5' 10-dT binding site for loading XPD and a 3' abasic site to prevent XD unwinding into the handle. All oligonucleotides were purchased from Integrated DNA Technologies (Coralville, IA).

Flow Chamber for Optical Tweezers Measurements. All measurements were carried out in laminar flow chambers described in Whitley *et al.* (36). Chambers were made from NescoFilm (Karlan, Phoenix, AZ) melted between two glass coverslips and laser-engraved with channels for buffers. Chambers for all measurements had three channels (**Figure 1—Figure Supplement 2**). Top and bottom channels contained anti-digoxigenin and DNA-coated streptavidin beads, respectively. Small (100-µm OD) glass capillaries connected the top and bottom channels to the central channel for trapping and allow a controlled flow of beads. Three separate streams converged into the central trapping channel. Because the flow in each stream is laminar, mixing between different buffer streams is minimal and a reasonably sharp boundary between buffer conditions was maintained (**Figure 1—Figure Supplement 2a**, inset). This chamber design allowed moving freely between different streams via motorized sample stage and changing buffer conditions during an experiment, as described below.

Optical trap measurements. High-resolution dual-trap optical tweezers based on a previously reported design (36,47) were used to study XPD helicase unwinding in the presence of RPA2. The optical traps were calibrated by standard procedures (36,48) and both traps had a typical stiffness of k = 0.3 pN/nm in all experiments. All data were acquired using custom LabVIEW software (National Instruments, Austin, TX), and were collected at a 267-Hz sampling rate and boxcar filtered to a lower frequency as indicated in the text. All measurements were carried out at a constant force of 12 pN using a feedback loop to maintain constant force.

1   *Fac*XPD and *Fac*RPA2 were purified as described previously by Pugh *et al*. (31). Single XPD unwinding

2   experiments were performed in a similar manner to that described in Qi *et al*. (33), with some

3   amendments. The trapping buffer consisted of 100 mM Tris-HCl (pH 7.6), 20 mM NaCl, 2 mM DTT, 3 mM

4   MgCl$_2$, 0.1 mg/mL BSA and oxygen scavenging system (49) (0.5 mg/mL pyranose oxidase [Sigma-Aldrich,

5   St. Louis, MO], 0.1 mg/mL catalase [Sigma-Aldrich, St. Louis, MO], and 0.4% glucose) to increase the

6   lifetime of the DNA tethers (50). To this buffer, varying concentrations of XPD, ATP, ATP-γS, and RPA2

7   were added. Unless otherwise noted, the following buffers filled the three laminar flow streams in the

8   central trapping channel (**Figure 1—Figure Supplement 2a**): Upper stream, 500 μM ATP + 0-50 nM RPA2;

9   Middle stream, 500 μM ATP-γS + 10 nM Cy3; Lower stream, 60 nM XPD + 500 μM ATP-γS. ATP-γS was

10   used to increase the binding efficiency of XPD to the DNA loading site. The dye molecule Cy3 was added

11   to the middle stream to detect, via fluorescence imaging, the precise locations of the middle stream

12   boundaries. Fluorescence detection of the Cy3 stream was achieved using a confocal microscope

13   incorporated into the optical trap instrument, as described in Refs. (36,47).

14   During a typical experiment, a single DNA hairpin was tethered between an optically trapped

15   streptavidin-coated bead and an anti-digoxigenin coated bead in the middle stream, in the absence of any

16   protein or ATP (Step 1 in **Figure 1—Figure Supplement 2b** and **2c**). A low force (~2 pN) was applied to the

17   tether, and the traps and tethered DNA were moved by motorized sample stage into the lower stream

18   containing XPD + ATP-γS, where they incubated for ~40-60 s to allow a single XPD to bind to the 10-dT

19   ssDNA loading site but not unwind the hairpin (Step 2). Following incubation, the force on the tether was

20   increased to 12 pN and the tether was moved into the upper stream containing ATP + RPA2 (Step 3). Upon

21   exposure to ATP, an XPD molecule bound at the loading site unwound the hairpin ahead of it, which, at

22   constant force, resulted in an increase in the end-to-end extension of the DNA tether (**Figure 1—Figure**

23   **Supplement 2c**). Unwinding data were typically collected until the tether broke or XPD dissociated.

24

25   **Analysis of DNA hairpins and determining base pairs unwound by XPD.** A force-extension curve of each

26   tether was usually taken in the middle stream containing no protein to verify proper synthesis. A properly

27   synthesized hairpin unzips mechanically at an applied force of ~15 pN (**Figure 1—Figure Supplement 1b**),

28   and its force-extension curve is well fit to the following model:

29   $$x(F) = N_{ds}\xi_{ds}(F) + N_{ss}\xi_{ss}(F),$$ (1)

30   where $\xi_{ds}(F)$ and $\xi_{ss}(F)$ are the extension of 1 bp of dsDNA and 1 nt of ssDNA at a given force, *F*,

31   respectively, and N_{ds} and N_{ss} are the number of dsDNA base pairs and ssDNA nucleotides, respectively, in

1   the construct. $\xi_{ds}(F)$ and $\xi_{ss}(F)$ are given by the extensible worm-like chain (XWLC) model of elasticity,

2   using the following parameters: persistence length P_{ds} = 50 nm and P_{ss} = 1.0 nm, contour length per base

3   pair/nucleotide h_{ds} = 0.34 nm bp^{-1} and h_{ss} = 0.59 nm nt^{-1}, and stretch modulus S_{ds} = 1,000 pN and S_{ss} = 1,000

4   pN (33,51). For the closed hairpin at forces <15 pN, the model Eq. (1) was used with N_{ds} = 3,050 bp,

5   corresponding to the sum of the handle lengths, and N_{ss} = 10 nt, corresponding to the helicase loading

6   site length (**Figure 1—Figure Supplement 1b**, black dashed line). For the open hairpin at forces >15 pN,

7   values N_{ds} = 3,050 bp and N_{ss} = 192 nt were used (**Figure 1—Figure Supplement 1b**, gray dashed line).

8   As a helicase unwinds the tethered DNA hairpin at a constant force, the tether extension increases

9   due to the release of 2 nt of ssDNA for each bp of the hairpin dsDNA unwound. The number of base pairs

10   unwound at each time point was obtained from the relation

11
$$n_{\text{unwound}}(t) = \frac{\Delta x(t)}{2\xi_{ss}(F)}, \qquad\qquad (2)$$

12   at the force F applied, and where Δx is the measured change in extension (in nm).

13

14   **Analysis of XPD unwinding bursts.** All XPD unwinding time traces were down-sampled from 267 Hz to 89

15   Hz. Start and end times for each unwinding burst were selected manually using the following criteria:

16   Bursts were defined as periods of significant forward progress by XPD (>5 bp) followed by significant

17   backward motion (>5 bp), excluding behavior obviously attributed to RPA2-mediated transient melting or

18   5-bp back- and forward step pairs XPD is known to take (33). The processivity (**Fig. 2c**) for each burst was

19   determined from the maximum number of base pairs open between the burst start and end time points,

20   and the burst duration (**Figure 4—Figure Supplement 2**) was determined from the time elapsed between

21   start and end time points.

22   For the analysis shown in **Fig. 4**, we considered only the unwinding portion of each burst. For highly

23   processive bursts, this segment consisted of the data from the beginning of the burst to the time point at

24   which the maximum number of base pairs was unwound. However, for low-processivity bursts that

25   exhibited extended stalls at ~10 bp, the unwinding endpoint was selected to be the last point above 10

26   bp. This allowed us to account for extended stalling behavior, while excluding rapid rezipping at the end

27   of the burst. For bursts with processivity less than 10 bp, the unwinding portion of each burst was selected

28   to be the first 75% of the total burst duration to exclude rapid rezipping at the end of the burst.

29

30   **Analysis of XPD unwinding speed.** To calculate the unwinding speed during each burst, we first smoothed

31   the data to remove any RPA2-mediated transient melting events. Data were smoothed over a 51-point

1   (190-ms) window using the weighted local regression method "rloess" in Matlab's in-built "smooth"

2   function, which fits the span around each data point to a 2nd degree polynomial and excludes outliers

3   based on a residual analysis. Then, the local velocity was determined over half-overlapping 50-point

4   windows from the slope of a fit of the data to a line. The corresponding times and hairpin positions were

5   also determined from their mean in each window. To create **Figure 4—Figure Supplement 1**, the local

6   velocity for each burst was plotted against hairpin position and averaged over the set of bursts analyzed.

7

8   **Analysis of RPA-mediated melting events.** RPA2-like melting events on the bare hairpin were identified

9   from short-lived melting of >4 bp of the hairpin (**Figure 3—Figure Supplement 2**). To find RPA2-like events

10   during XPD unwinding, we identified steps in selected XPD unwinding bursts using an algorithm by

11   Kerssemakers *et al.* (52) (**Figure 3—Figure Supplement 2a**). Specifically, we searched for adjacent pairs of

12   steps that met the following criteria: >2 bp forward step (step *n*) followed by >2 bp back-step (step *n*+1)

13   within 5 time points (56 ms) of each other (**Figure 3—Figure Supplement 2b** outlined in red). While false

14   positives are observable even in the absence of RPA2, their probability is low, and the probability increases

15   with RPA2 concentration (**Figure 3—Figure Supplement 2c**), confirming their connection to RPA2 activity.

16   Each step was then aligned at full bandwidth (267 Hz) to the detected locations of RPA2 melting and

17   reannealing. We used 2D kernel density estimation to visualize the probability density of these aligned

18   traces. In this method, each point in the aligned data was replaced by a kernel function, here a 2D

19   Gaussian. The sum of all kernels provides an excellent approximation to the probability density. The darker

20   color in **Fig. 3e** and **f** indicate higher probability.

21

22   **Kinetic model.** We defined a model in which XPD can exist in two intrinsic states—a low- and high-

23   processivity state—the latter of which we infer only when XPD unwinds past a ~25 bp threshold. In this

24   model, XPD can alternate between "low" and "high" states (with rates constants k_1 and k_{-1}) and can also

25   dissociate from DNA from both states (with rates constants k_{off} and k'_{off}, respectively; **Fig. 5a**). The effect

26   of RPA2 increasing the probability of the high-processivity state is captured by the dependence of the rate

27   constant k_1 on [RPA2]. Since the high-processivity state is "hidden", and unwinding bursts are scored as

28   high processivity only when XPD unwinds >25 bp, the model includes the rate constant k_2 that determines

29   the time XPD takes to pass this threshold.

30   We used this kinetic model to fit the measured first-passage-time for XPD to unwind past 25 bp. The

31   model in **Figure 5a** is described by a set of master equations for the state probabilities:

$$\dot{P}_{low}(t) = k_{-1}P_{high}(t) - (k_{off} + k_1)P_{low}(t)$$

1
$$\dot{P}_{high}(t) = k_1 P_{low}(t) - (k'_{off} + k_{-1} + k_2)P_{high}(t)$$

$$\dot{P}_{off}(t) = k_{off}P_{low}(t) + k'_{off}P_{high}(t)$$

$$\dot{P}_{>25}(t) = k_2 P_{high}(t)$$

2 where the subscripts correspond to the four possible states: low processivity ("low"), high processivity

3 ("high"), dissociated ("off"), and past the 25 bp threshold (">25"). The first passage time is measured from

4 the time XPD is first exposed to RPA2, and XPD is in the low-processivity state. Thus, the initial conditions

5 are given by:

6 $$P_{low}(0) = 1; \quad P_{high}(0) = 0; \quad P_{off}(0) = 0; \quad P_{>25}(0) = 0$$

7 These coupled linear differential equations can be solved to determine all four state probabilities. Here,

8 we provide an expression for $P_{>25}$, which is plotted in **Fig. 5c**:

9 $$P_{>25}(t) = \frac{k_1 k_2}{\lambda_- - \lambda_+} \left(\frac{1 - e^{-\lambda_+ t}}{\lambda_+} - \frac{1 - e^{-\lambda_- t}}{\lambda_-} \right).$$

10 The eigenvalues of the system give the decay constants for the exponentials:

11 $$\lambda_{\pm} = \frac{k_1 + k_{-1} + k_2 + k_{off} + k'_{off}}{2} \pm \left[\left(\frac{k_1 + k_{-1} + k_2 + k_{off} + k'_{off}}{2} \right)^2 - \left(k_1(k_2 + k'_{off}) + k_{off}(k_{-1} + k'_{off}) \right) \right]^{1/2}.$$

12 In our model, only k_1 is expected to vary as a function of RPA concentration. By grouping terms that are

13 RPA-concentration dependent vs. independent, $P_{>25}(t)$ can be written in terms of 5 unknown parameters

14 A, B, C, D, and k related to the 5 rate constants:

15 $$P_{>25}(t,[RPA2]) = \frac{k([RPA2])D}{\lambda_- - \lambda_+} \left(\frac{1 - e^{-\lambda_+ t}}{\lambda_+} - \frac{1 - e^{-\lambda_- t}}{\lambda_-} \right), \qquad (3)$$

16 and

17 $$\lambda_{\pm} = \frac{k([RPA2]) + B + C}{2} \pm \left[\left(\frac{k([RPA2]) + B + C}{2} \right)^2 - \left(Ak([RPA2]) + BC \right) \right]^{1/2}, \qquad (4)$$

18 where k is written explicitly as a function of [RPA2]. The relationships between the 5 parameters and rate

19 constants are given by:

20 $$k_1 = k([RPA2]); \quad k_2 = D; \quad k_{-1} = C - A; \quad k'_{off} = A - D; \quad k_{off} = B.$$

21 We performed a global fit to our first-passage-time data (**Fig. 5c**) using Eq. (3) and (4) with common

22 values A, B, C, and D for all RPA2 concentrations but a different value for $k([RPA2])$ at each concentration

23 (**Fig. 5d**). In the data fit displayed in **Figure 5c** (dashed line), we set k'_{off} to zero; we found that the best-fit

16

1   value for k'_{off} was small with a large error (-0.05 ± 1.23) and provided no significant improvement to the

2   fit. By assuming k'_{off} = 0, *A = D*, reducing our fit to 4 parameters: *A, B, C, k*. Parameter values and

3   uncertainties are listed in **Table 2**.

4   In addition, we used Eq. (3) to model the RPA2-dependent fraction of high-processivity bursts (**Fig.**

5   **4b**) and average burst duration (**Figure 4—Figure Supplement 2**). For the former, data were fit to the

6   expression for $P_{>25}(t)$ evaluated at a time *t* equal to the average low-processivity burst duration τ_{low} = 7 s.

7   The latter was fit to the following model:

8    $$\langle t_{burst} \rangle = \tau_{low}\left(1 - P_{>25}(t \rightarrow \infty, [\text{RPA2}])\right) + \tau_{high}P_{>25}(t \rightarrow \infty, [\text{RPA2}]),$$

9   in which the average burst duration is given by the sum of the low-processivity burst duration, τ_{low}, and

10   the high-processivity burst duration, τ_{high}, multiplied by the probabilities of being in their respective states

11   at long times ($t \rightarrow \infty$):

12   $$P_{>25}(t \rightarrow \infty, [\text{RPA2}]) = \frac{k[\text{RPA2}]D}{k[\text{RPA2}]A + BC}.$$

17
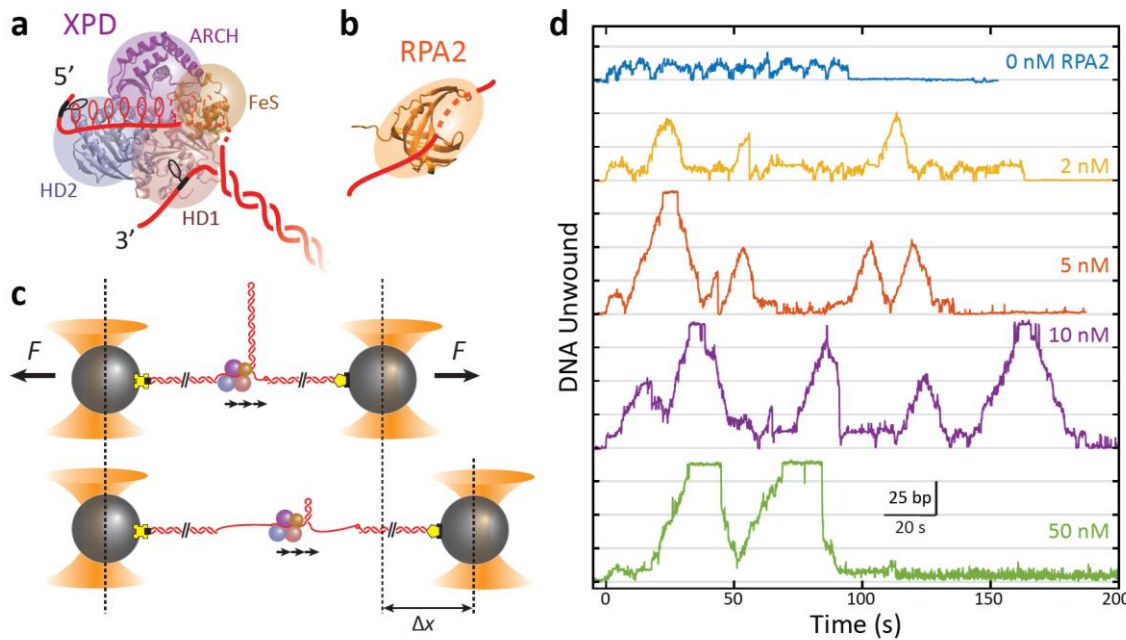
1 **Figures**

3 **Figure 1. RPA2 increases XPD helicase processivity. a** Schematic of *Fac*XPD based on *S. acidocaldarius*

4 XPD structure (PDB 3CRV). XPD is composed of four domains: Helicase Domain 1 and 2 (HD1, blue; HD2,

5 pink) which form the motor core, and the ARCH domain (purple) and FeS cluster (brown). A model of the

6 DNA fork (red) shows ~10 nt bound to the motor core and secondary contacts (black) to each strand of

7 the fork. **b** Schematic of *Fac*RPA2 based on partial crystal structure of *M. maripaludis* RPA (PDB 2K5V).

8 RPA2 consists of a single OB fold that binds to ssDNA in the C-shaped cavity. **c** Single-molecule hairpin

9 unwinding assay. A DNA hairpin consisting of an 89-bp stem and $(dT)_4$ loop is tethered between trapped

10 beads by biotin-streptavidin (yellow cross) and digoxigenin-antibody linkages (pentagon) and held at a

11 constant force. A 10-nt poly-dT site at the 5' end of the hairpin allows one XPD molecule to load, and an

12 abasic site at the 3' end prevents XPD unwinding past the hairpin. Unwinding of the hairpin by XPD

13 increases the end-to-end extension of the construct by an amount, Δx, proportional to the number of base

14 pairs unwound. Arrows indicate the 5' to 3' direction of XPD translocation along ssDNA. **d** Representative

15 traces of a single molecule of XPD unwinding in the presence of varying concentrations of RPA2 (0-50 nM)

16 at constant force (F = 12 pN). ATP and RPA2 are added at t = 0 s. XPD processivity increases with RPA2

17 concentration.
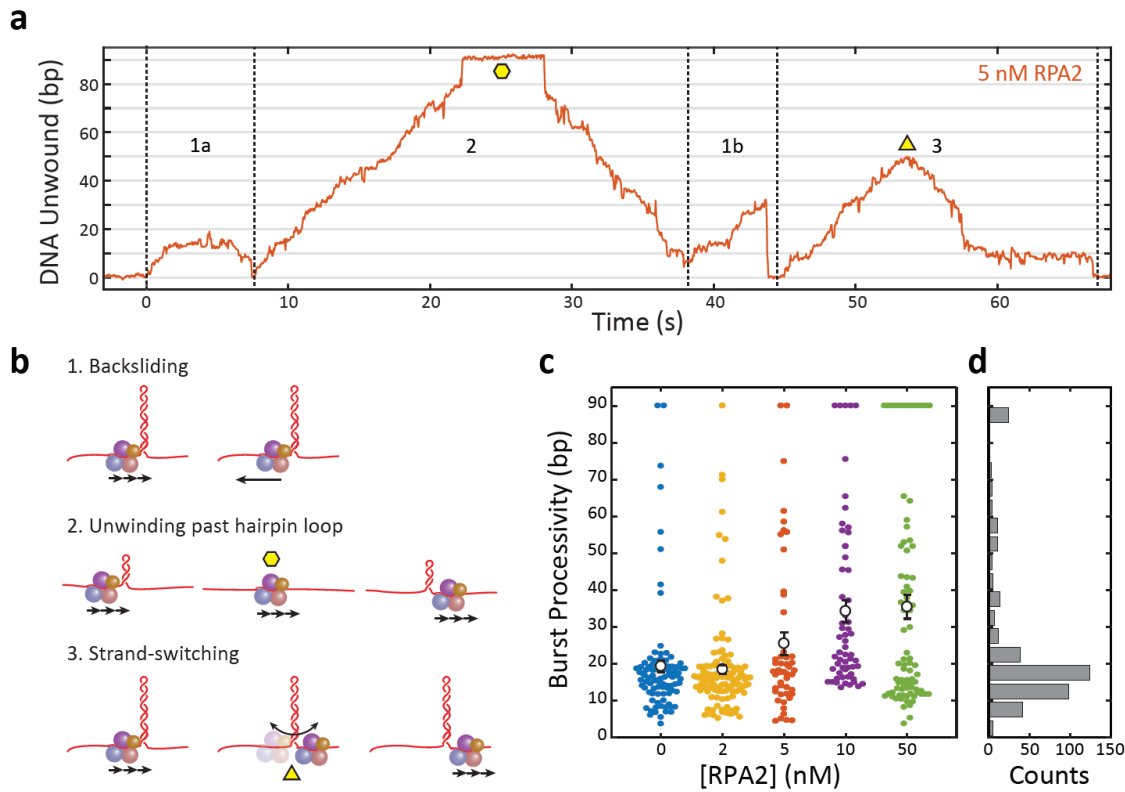
Figure 2. XPD unwinds in bursts of varying processivity whose average increases with RPA2 concentration. a Representative trace of a single molecule of XPD unwinding in the presence of RPA2 (5 nM). One XPD exhibits repetitive bursts of activity, making multiple attempts to unwind hairpin DNA. Processivity can vary widely from burst to burst. Example time trace with: (1a) 20 bp- and (1b) 30 bp-processivity bursts composed of forward unwinding followed by backsliding to the hairpin base; (2) a high-processivity burst during which XPD completely unwinds the 90-bp hairpin past the hairpin loop (time point indicated by yellow hexagon) and translocates on the opposing strand, allowing the hairpin to rezip; and (3) a 50 bp-processivity burst during which XPD unwinds and switches strand mid-hairpin (indicated by yellow triangle), allowing the hairpin to rezip. **b** Schematics representing the behaviors in (a). **c** Processivity of each burst (colored circles) vs. RPA2 concentration. The mean processivity (open circles) increases with RPA2 concentration. Error bars represent s.e.m. **d** Histogram of all burst processivities at all RPA2 concentrations.

19

1
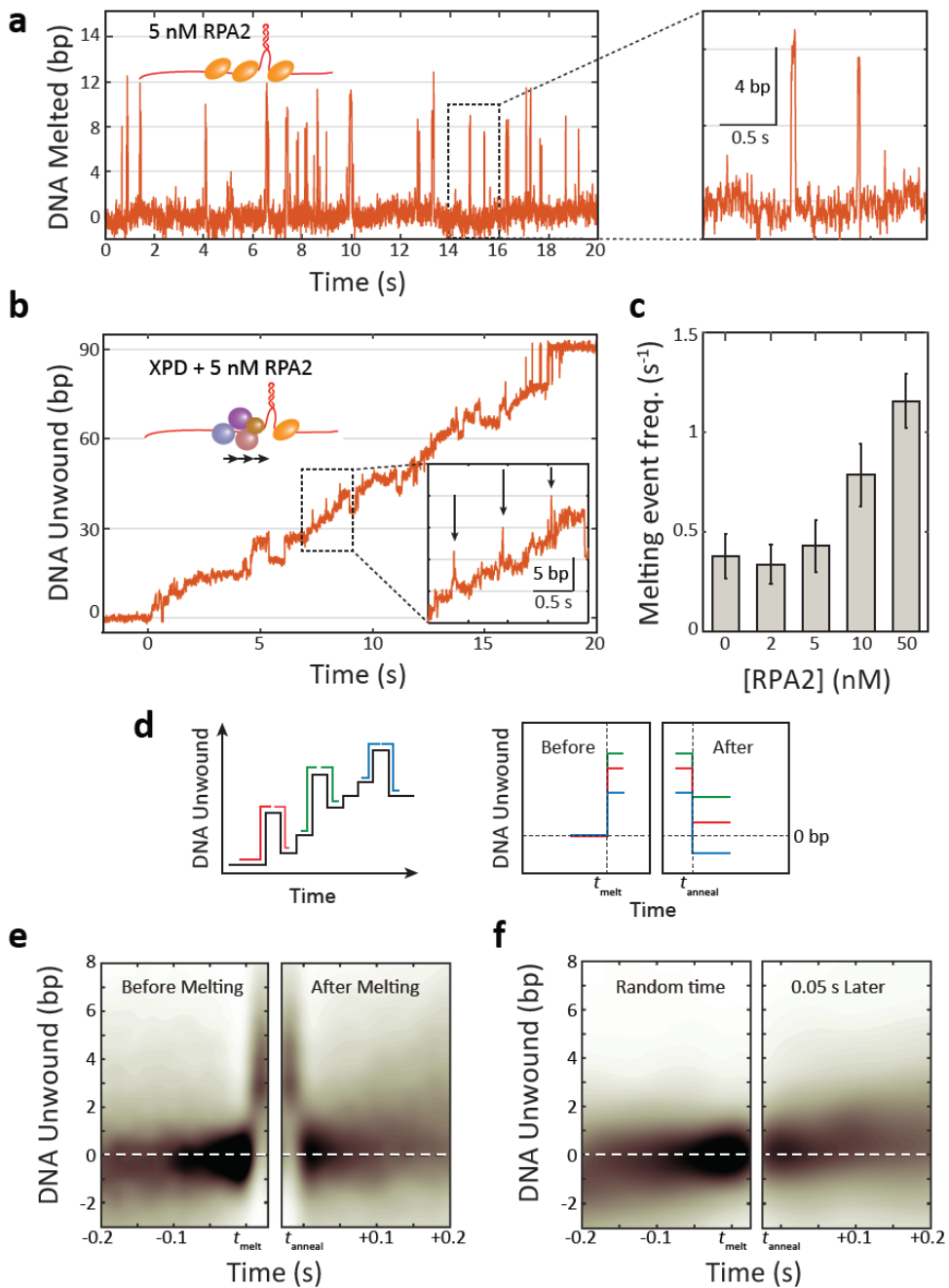
Figure 3. RPA2 transiently melts hairpin duplex but does not assist XPD unwinding. a Representative time trace of RPA2 transiently destabilizing hairpin dsDNA at a constant force (F = 12 pN). Inset: RPA2 melts ~8 bp, which then rapidly reanneals (see Figure 3—Figure Supplement 1). **b** RPA2 is able to melt dsDNA at a fork occupied with XPD. Inset: transient RPA2-like melting events during XPD unwinding (see Figure 3—Figure Supplement 2). **c** The frequency of RPA2 melting events increases with RPA2 concentration. Error bars represent s.e.m. **d** Analysis of RPA2 melting events and their effect on XPD

1   unwinding. The schematic shows all RPA2 melting events identified and divided into "melting" and

2   "reannealing" transitions. Each transition is aligned temporally such that all melting transitions begin at

3   the same time t_{melt} and corresponding reannealing transitions end at the same time t_{anneal}. Both types of

4   transitions are aligned spatially relative to the starting extension before melting (x = 0). **e** Probability

5   distribution of all aligned RPA2 melting events. Although RPA2 melts an average of 5 bp of hairpin DNA

6   (left), it reanneals by the same amount (right), and there is no net progress of XPD due to melting. **f**

7   Probability distribution at a random time point (left) and 0.06 s later (right). Net progress of XPD after an

8   RPA2 melting event is indistinguishable from net progress at a random time point. Probability distributions

9   were obtained using kernel density estimation (see Methods).
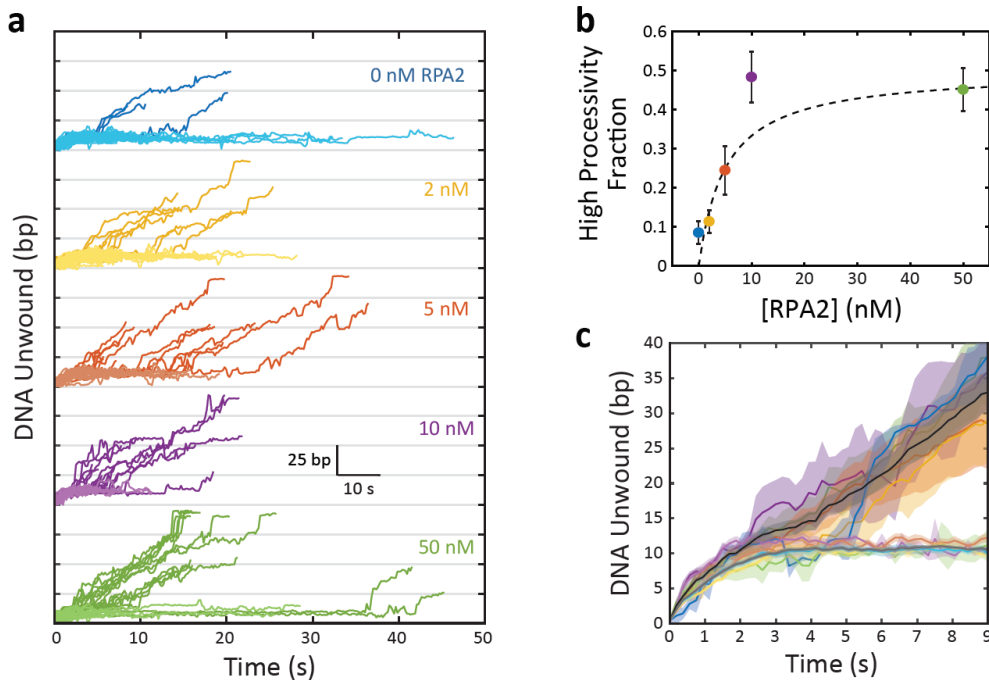
1

Figure 4. XPD exhibits two burst types, the fraction of which is RPA2 dependent. a Plot of XPD unwinding bursts, aligned to start at $t = 0$ and grouped by RPA2 concentration (colored traces). XPD unwinding bursts come in two types: low processivity, never unwinding more than 25 bp, (light colors); and high processivity, unwinding more than 25 bp (dark colors). **b** The fraction of high-processivity bursts (>25 bp) increases with RPA2 concentration. Fit to model described in the text (dashed line; see Methods). **c** Averages of all low-processivity bursts (light colored lines) and all high-processivity bursts (dark colored lines) at each RPA2 concentration. Comparison to averages of low- and high-processivity burst types over all RPA2 concentrations (dark gray and black lines, respectively). Shaded regions represent s.e.m. throughout. Unwinding behavior within each burst category remains the same over all RPA2 concentrations.
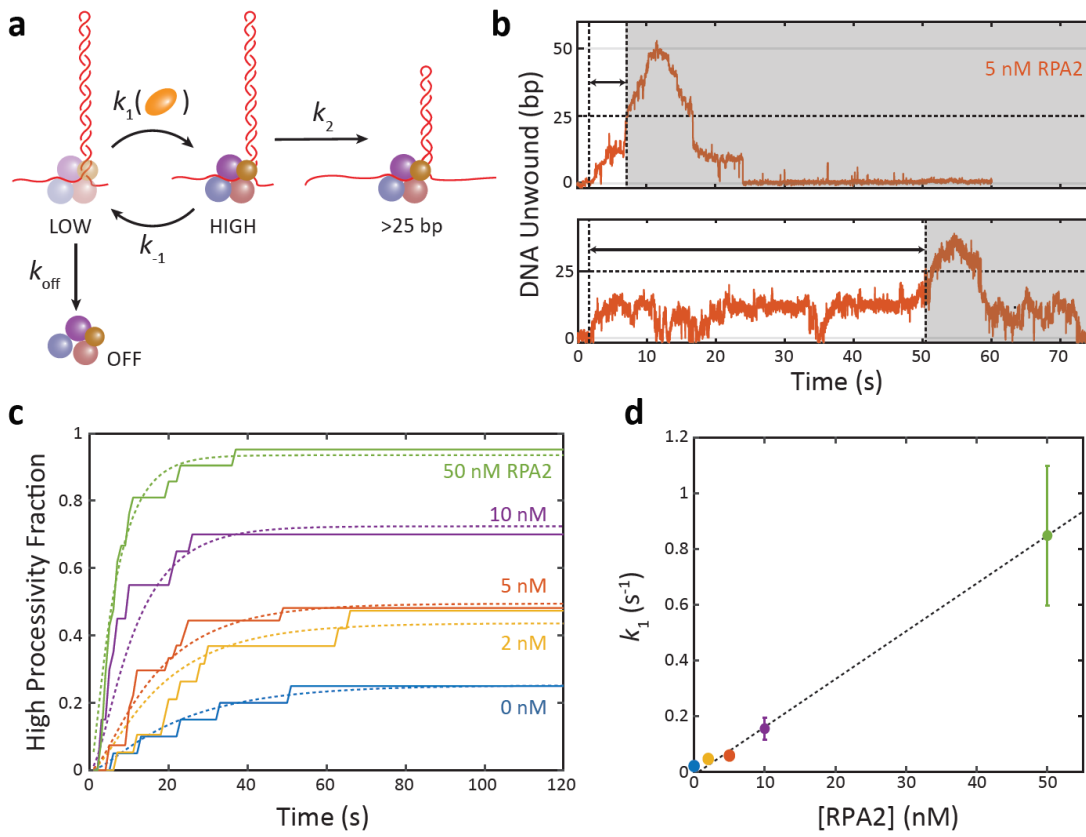
22

Figure 5. RPA2 activates a high processivity state of XPD. a Kinetic model of XPD processivity and the effect of RPA2. XPD can adopt one of two intrinsic states—a LOW and HIGH processivity state. XPD interconverts between both states with rates k_1 and k_{-1}, and RPA2 shifts the equilibrium toward the HIGH state. XPD can dissociate from DNA only from the LOW state with rate k_{off}. Only in the HIGH state is XPD able to unwind in excess of 25 bp, which occurs at a rate k_2. Once an XPD molecule unwinds >25 bp, it is scored as being in the HIGH processivity state. **b** Representative traces of XPD exhibiting high processivity unwinding. The time $t_{>25}$ denotes the first time at which XPD crosses the 25 bp threshold. **c** Fraction of all XPD molecules that have reached high processivity (>25 bp) after time t for each RPA2 concentration. The curves are globally fit to the model in (a) using as parameters the rate constants k_1, k_{-1}, k_2, and k_{off}. **d** The rate of entry into the high processivity state, k_1, depends linearly on RPA2 concentration. For more details on the kinetic model see Methods.

23

1   **Figure Supplements**
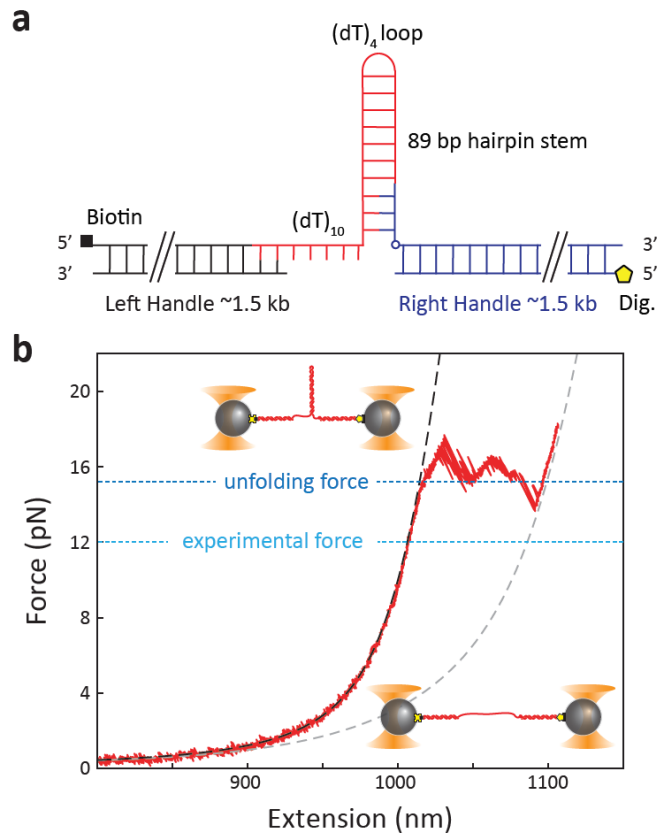
2

3   **Figure 1—Figure Supplement 1. DNA hairpin construct. a** The hairpin construct consists of three ligated

4   DNA fragments: left (black) and right (blue) dsDNA handles and an 89-bp hairpin that includes a 5' 10-nt

5   ssDNA protein loading site. The left and right handles are modified with a 5' biotin (black square) and 5'

6   digoxigenin (yellow pentagon), respectively, for attachment to beads. **b** Representative force-extension

7   curve of a DNA hairpin. The experimental curve (red solid line) is fit to a model of the closed (black dashed

8   line) and open (gray dashed line) hairpin. (See Methods).

24

1
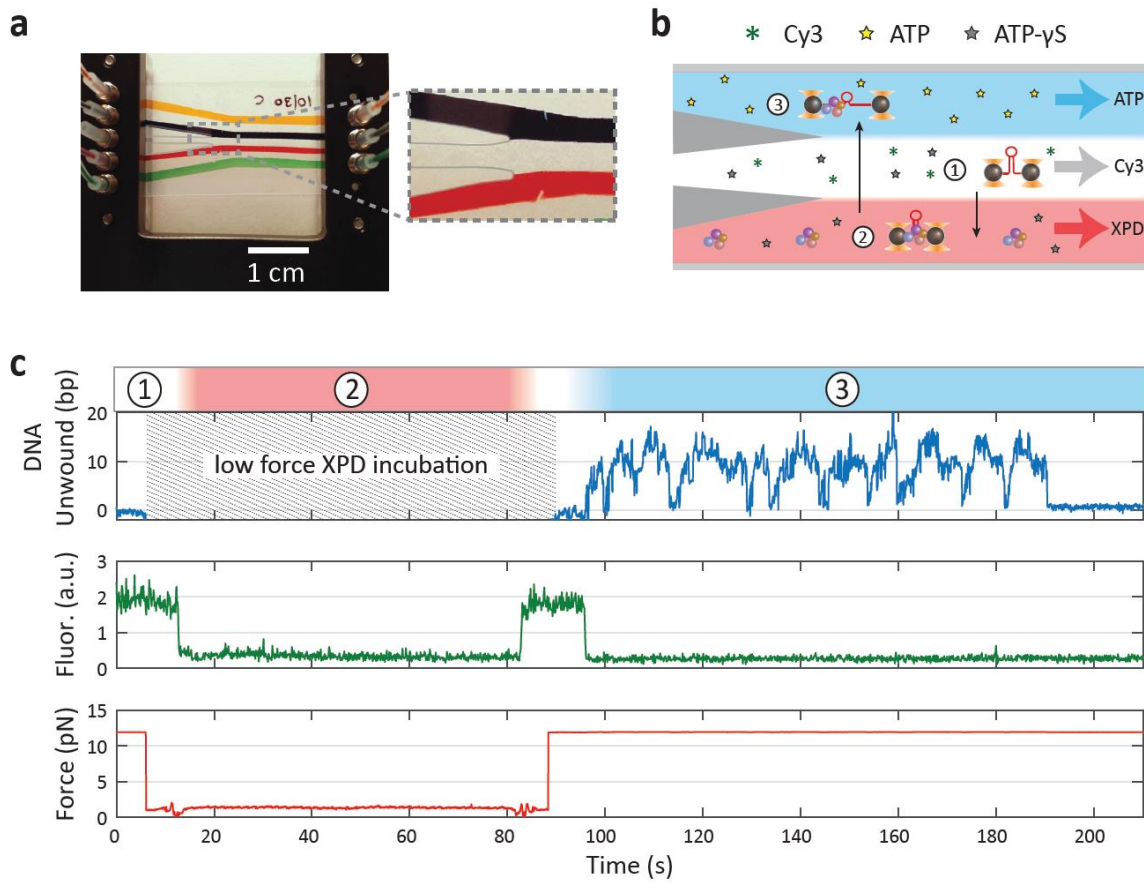
2 **Figure 1—Figure Supplement 2. Laminar flow chamber. a** Photograph of laminar flow chamber. Colored

3 food dye highlights the different flow streams. Parafilm in the central channel is recolored to enhance

4 contrast. The bead channels (yellow and green) are connected via capillaries to the central trapping region

5 (inset). Three streams (dark blue, uncolored, and red) meet in the center channel but mix minimally. **b**

6 Typical experimental protocol. The upper stream of the the central channel is filled with buffer containing

7 500 μM ATP, the middle stream with 500 μM ATP-γS, and the bottom stream with 60 nM XPD and 500

8 μM ATP-γS. The dye Cy3 is added to the middle stream for illustrative purposes. A DNA hairpin is tethered

9 between trapped beads in the middle stream (step 1), and its force-extension behavior characterized (see

10 Figure 1—Figure Supplement 1). The trapped beads and DNA are next moved into the XPD stream (step

11 2) for ~1 min. for a single XPD to bind at low force, ~1-2 pN. Then, they are moved into the ATP stream

12 (step 3) to initiate XPD unwinding, as the force is increased and maintained at 12 pN. **c** Example unwinding

13 trace of a single XPD. Colored regions and numbers above the trace correspond to chamber locations in

14 b. Cy3 fluorescence intensity indicates when the traps are in the middle stream. Unwinding activity begins

15 as soon as XPD enters the ATP stream (t = 95 s). XPD unwinds in repetitive "bursts" of activity for ~90 s

16 until it dissociates.

25
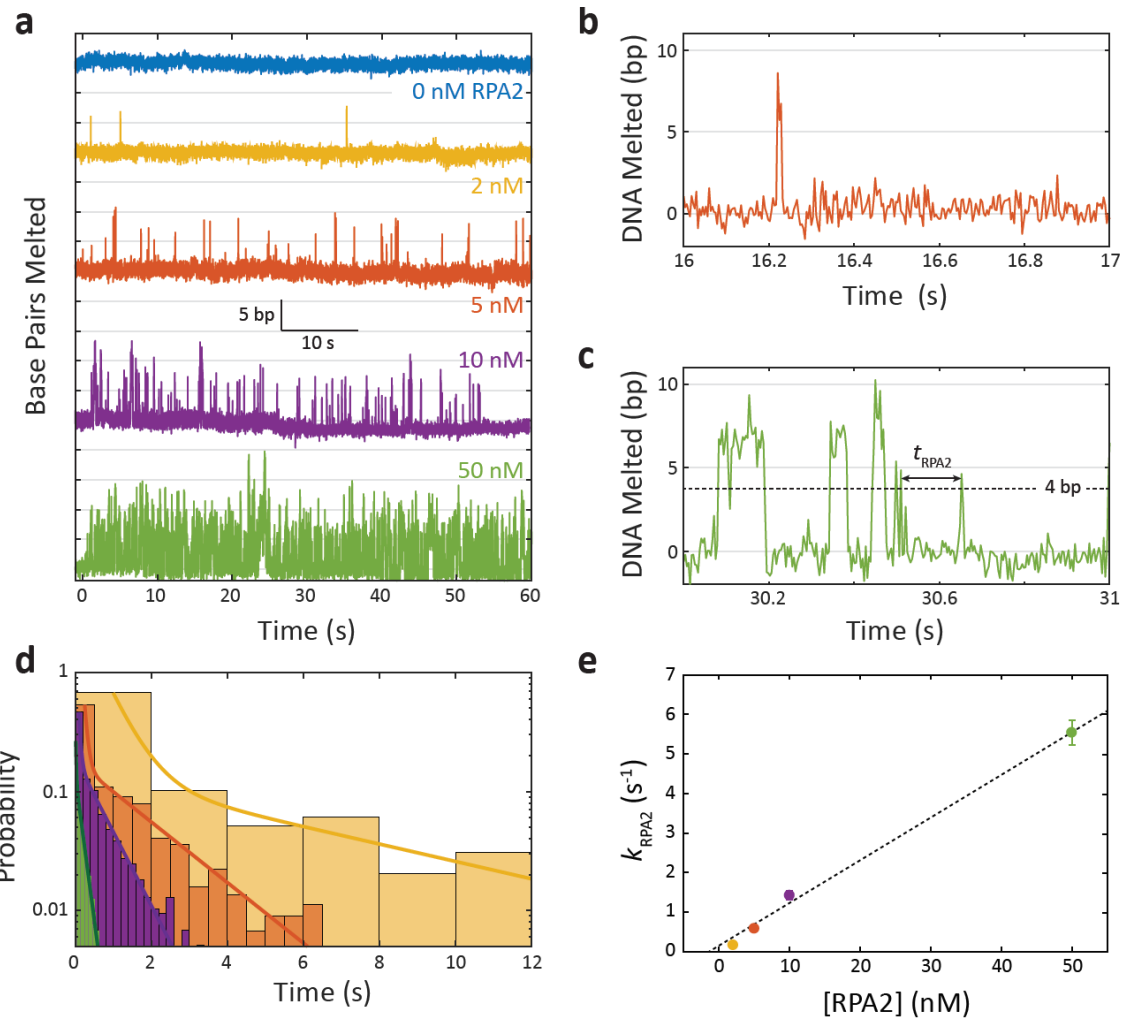
Figure 3—Figure Supplement 1. RPA2 transiently melts DNA under force. a Representative time traces of RPA2 transiently destabilizing hairpin dsDNA at a constant force (F = 12 pN) and at varying RPA2 concentrations. The hairpin is exposed to varying concentrations of RPA2 at t = 0. In the absence of RPA2, the hairpin remains stably zipped. In the presence of RPA2, brief (<0.1 s) events consisting of 5-10 bp dsDNA melting followed by rapid reannealing are observed. The frequency of these events increases with RPA2 concentration. **b-c** Selected RPA2 melting events from traces in a with 5 nM and 50 nM RPA2. Melting events are identified at time points where >4 bp of DNA is unwound, and melting kinetics are quantified from the time between events, t_{RPA2}. **d** Probability distribution of t_{RPA2} across RPA2 concentrations (colors same as in a). The distributions are best fit to a bi-exponential with one slow and one fast rate constant. The slow process depends on [RPA2] and corresponds to RPA2 binding and melting the hairpin DNA. The fast process is independent of [RPA2] (data not shown), and attributed to already-

26

1   bound RPA2 "re-melting" the DNA. **e** The effective RPA2 binding rate, k_{RPA2}, determined from the slow

2   rate constant in d, increases linearly with RPA2 concentration. Error bars represent s.e.m.
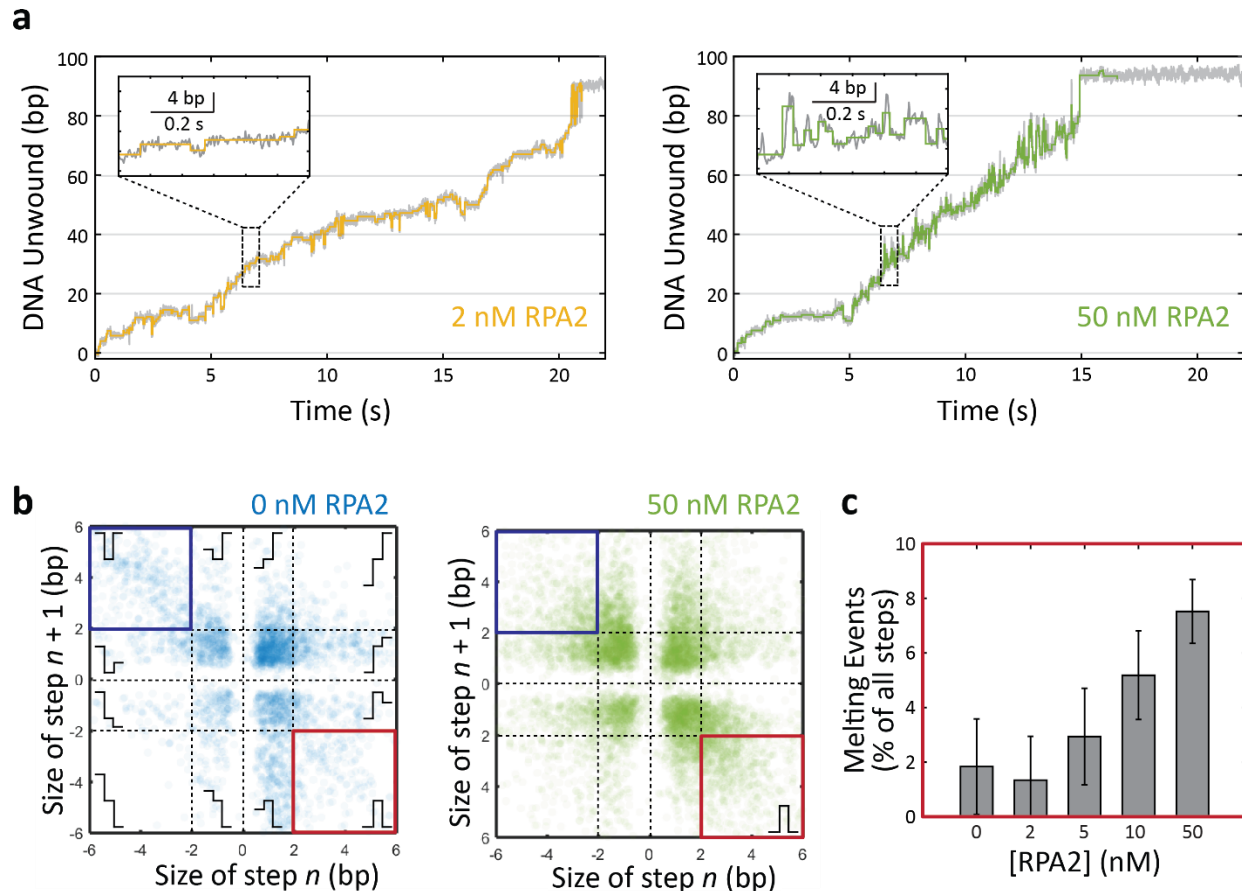
Figure 3—Figure Supplement 2. Detecting RPA2 melting events during XPD unwinding. **a** Representative time traces of XPD unwinding in the presence of 2 nM and 50 nM RPA2 (data in gray) and corresponding step-fitting analysis (colored line) used to identify putative RPA2 melting events. Inset: steps fitted (colored lines) to unwinding data (gray). **b** Scatter plot of step size for pairs of consecutive steps for XPD unwinding in 0 and 50 nM RPA2 (blue and green, respectively). Schematics illustrate the step pairs. In the absence of RPA2, small steps (<2 bp) account for the majority of unwinding behavior. In the presence of RPA2, a detectable fraction of step pairs corresponds to a large (>2 bp) forward step followed by a large backward step (red outline; lower right corner). A subset of these events with the appropriate duration (~0.06 s) are selected as RPA2 melting events. Step pairs consisting of a ~5-bp backward step followed by a forward step (dark blue outline; upper left corner) are attributed to DNA dynamics at a secondary, regulatory binding site on XPD. These events are less frequent in the presence of RPA2 (compare 0 nM and 50 nM RPA2; see Discussion). **c** The probability of RPA2 melting events identified in b increases with RPA2 concentration, confirming their connection to RPA2 activity. Some events are detected in the absence of RPA2 due to detection errors. Error bars represent s.e.m.

28

1
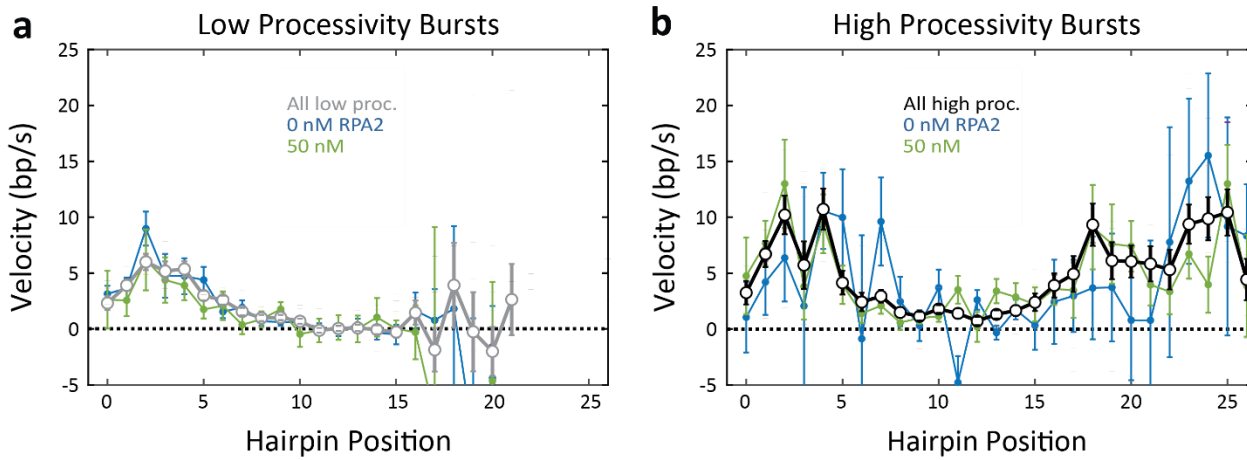
Figure 4—Figure Supplement 1. Unwinding velocity varies with processivity type but not RPA2 concentration. a-b Average unwinding velocity as a function of hairpin position for low-processivity (a) and high-processivity (b) bursts at two representative RPA2 concentrations, 0 (blue) and 50 nM (green). Velocities averaged over all RPA2 concentration for high- and low- processivity burst types are shown for comparison (black and gray, respectively). Velocity profiles are similar within each processivity type, independent of RPA2 concentration. However, velocity profiles for high processivity bursts differ significantly from those of low processivity bursts, particularly at positions >10 bp. Error bars represent s.e.m.

1
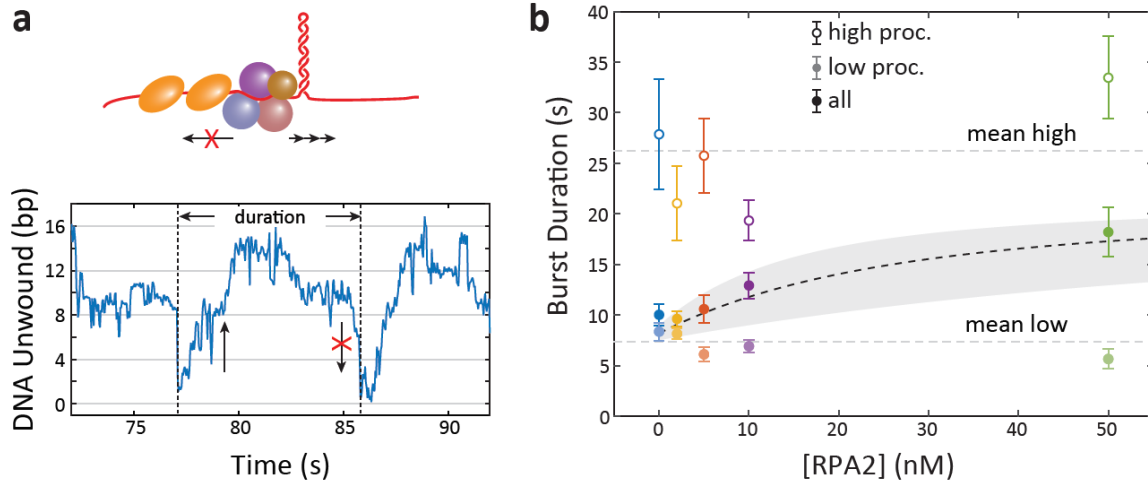
3 **Figure 4—Figure Supplement 2. XPD backward motion varies with processivity type but not RPA2**

4 **concentration. a** Schematic representation of the sequestration model, in which RPA2 binding to ssDNA

5 prevents XPD's backward motion, enhancing unwinding. The model predicts that burst duration should

6 increase with RPA2 concentration, since each burst ends when backward motion takes XPD to the base of

7 the hairpin. **b** Average burst duration for low-processivity (gray circles) and high-processivity (open circles)

8 remains constant with RPA2 concentration. Burst durations averaged over both burst types (black circles)

9 increases with RPA2 due to the increasing fraction of high-processivivity bursts, consistent with the

10 quantitative model (shaded gray region) based on Figure 4b (see Methods).

1
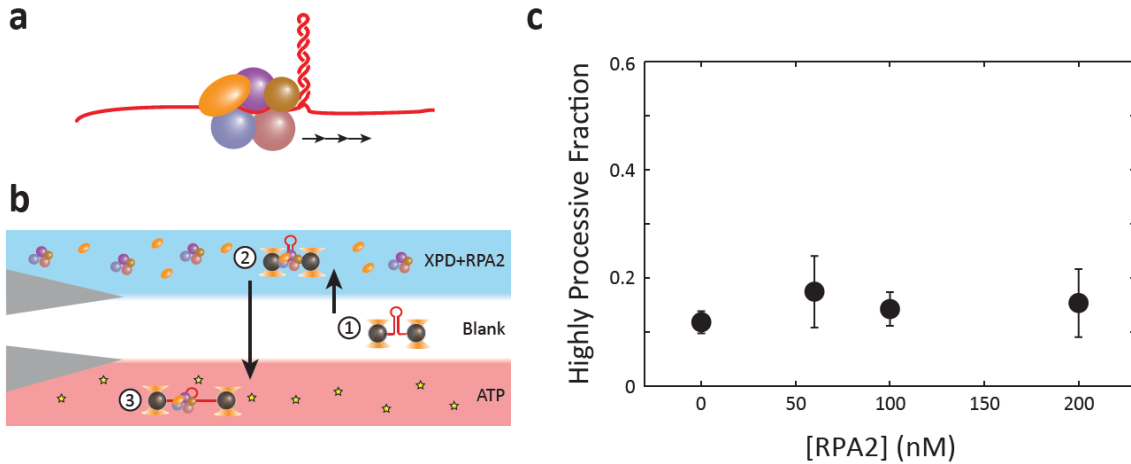
Figure 5—Figure Supplement 1. Test of stable complex formation. a In the complex formation model, RPA2 forms a complex with XPD that activates it for processive unwinding. **b** Flow chamber configuration for testing the complex formation model. The protein stream contains 60 nM XPD, 500 μM ATP-γS, and 0 – 200 nM RPA2. This configuration allows pre-loading an XPD-RPA2 complex during incubation. Unwinding processivity of the putative complex is measured upon entering into the ATP stream. **c** Although an XPD-RPA2 complex is predicted to be more likely as RPA2 concentration increases, the high processivity fraction remains constant with increasing RPA2 concentration. Error bars represent s.e.m. ($N = 6 - 43$ molecules).

1   **Tables**

Parameter	[RPA2] = 0	2 nM	5 nM	10 nM	50 nM
No. of XPD molec.	20	19	27	20	21
No. of bursts	94	123	79	60	82
No. of bursts/XPD	4.7	6.5	2.9	3.0	3.9
No. of low-proc. bursts	86	109	61	31	45
No. of high-proc. bursts	8	14	18	29	37

2   **Table 1. Data statistics.**

Rate const.	Fit value (s^{-1})
k_{-1}	0.18 ± 0.13
k_2	0.170 ± 0.017
k_{off}	0.037 ± 0.019
k'_{off}	0
k_1, [RPA2] = 0 nM	0.02 ± 0.006
k_1, 2 nM	0.059 ± 0.017
k_1, 5 nM	0.065 ± 0.019
k_1, 10 nM	0.200 ± 0.059
k_1, 50 nM	1.15 ± 0.39

3   **Table 2. Model fit parameters.** Error bars represent 95% confidence intervals.

References

1. Delagoutte, E. and von Hippel, P.H. (2002) Helicase mechanisms and the coupling of helicases within macromolecular machines. Part I: Structures and properties of isolated helicases. *Q Rev Biophys*, **35**, 431-478.

2. Delagoutte, E. and von Hippel, P.H. (2003) Helicase mechanisms and the coupling of helicases within macromolecular machines. Part II: Integration of helicases into cellular processes. *Q Rev Biophys*, **36**, 1-69.

3. Singleton, M.R., Dillingham, M.S. and Wigley, D.B. (2007) Structure and mechanism of helicases and nucleic acid translocases. *Annu Rev Biochem*, **76**, 23-50.

4. Lohman, T.M., Tomko, E.J. and Wu, C.G. (2008) Non-hexameric DNA helicases and translocases: mechanisms and regulation. *Nat Rev Mol Cell Biol*, **9**, 391-401.

5. McGlynn, P. (2013) Helicases at the replication fork. *Adv Exp Med Biol*, **767**, 97-121.

6. Daley, J.M., Niu, H. and Sung, P. (2013) Roles of DNA helicases in the mediation and regulation of homologous recombination. *Adv Exp Med Biol*, **767**, 185-202.

7. Kuper, J. and Kisker, C. (2013) DNA Helicases in NER, BER, and MMR. *Adv Exp Med Biol*, **767**, 203-224.

8. Wu, C.G. and Spies, M. (2013) Overview: what are helicases? *Adv Exp Med Biol*, **767**, 1-16.

9. Beyer, D.C., Ghoneim, M.K. and Spies, M. (2013) Structure and Mechanisms of SF2 DNA Helicases. *Adv Exp Med Biol*, **767**, 47-73.

10. Fairman-Williams, M.E., Guenther, U.P. and Jankowsky, E. (2010) SF1 and SF2 helicases: Family matters. *Curr Opin Struct Biol*, **20**, 313-324.

11. Byrd, A.K. and Raney, K.D. (2012) Superfamily 2 helicases. *Frontiers in bioscience (Landmark edition)*, **17**, 2070-2088.

12. White, M.F. and Dillingham, M.S. (2012) Iron-sulphur clusters in nucleic acid processing enzymes. *Curr Opin Struct Biol*, **22**, 94-100.

13. Egly, J.M. and Coin, F. (2011) A history of TFIIH: two decades of molecular biology on a pivotal transcription/repair factor. *DNA Repair (Amst)*, **10**, 714-721.

14. Fuss, J.O. and Tainer, J.a. (2011) XPB and XPD helicases in TFIIH orchestrate DNA duplex opening and damage verification to coordinate repair with transcription and cell cycle via CAK kinase. *DNA Repair (Amst)*, **10**, 697-713.

15. Kuper, J., Braun, C., Elias, A., Michels, G., Sauer, F., Schmitt, D.R., Poterszman, A., Egly, J.-M. and Kisker, C. (2014) In TFIIH, XPD Helicase Is Exclusively Devoted to DNA Repair. *PLoS biology*, **12**, e1001954.

16. Houten, B.V., Kuper, J. and Kisker, C. (2016) Role of XPD in cellular functions: To TFIIH and beyond. *DNA Repair (Amst)*, **44**, 136-142.

17. Ito, S., Tan, L.J., Andoh, D., Narita, T., Seki, M., Hirano, Y., Narita, K., Kuraoka, I., Hiraoka, Y. and Tanaka, K. (2010) MMXD, a TFIIH-independent XPD-MMS19 protein complex involved in chromosome segregation. *Mol Cell*, **39**, 632-640.

18. Yoder, K., Sarasin, A., Kraemer, K., McIlhatton, M., Bushman, F. and Fishel, R. (2006) The DNA repair genes XPB and XPD defend cells from retroviral infection. *Proc Natl Acad Sci U S A*, **103**, 4622-4627.

19. Fan, L., Fuss, J.O., Cheng, Q.J., Arvai, A.S., Hammel, M., Roberts, V.A., Cooper, P.K. and Tainer, J.A. (2008) XPD helicase structures and activities: insights into the cancer and aging phenotypes from XPD mutations. *Cell*, **133**, 789-800.

20. Liu, H., Rudolf, J., Johnson, K.A., McMahon, S.A., Oke, M., Carter, L., McRobbie, A.M., Brown, S.E., Naismith, J.H. and White, M.F. (2008) Structure of the DNA Repair Helicase XPD. *Cell*, **133**, 801-812.

21. Wolski, S.C., Kuper, J., Hänzelmann, P., Truglio, J.J., Croteau, D.L., Houten, B.V. and Kisker, C. (2008) Crystal Structure of the FeS Cluster–Containing Nucleotide Excision Repair Helicase XPD. *PLoS biology*, **6**, 1332-1342.

22. Kuper, J., Wolski, S.C., Michels, G. and Kisker, C. (2012) Functional and structural studies of the nucleotide excision repair helicase XPD suggest a polarity for DNA translocation. *The EMBO Journal*, **31**, 494-502.

23. Spies, M. (2014) Two steps forward, one step back: determining XPD helicase mechanism by single-molecule fluorescence and high-resolution optical tweezers. *DNA Repair (Amst)*, **20**, 58-70.

24. Shereda, R.D., Kozlov, A.G., Lohman, T.M., Cox, M.M. and Keck, J.L. (2008) SSB as an organizer/mobilizer of genome maintenance complexes. *Crit Rev Biochem Mol Biol*, **43**, 289-318.

25. Spies, M. and Ha, T. (2010) Inching over hurdles: how DNA helicases move on crowded lattices. *Cell cycle (Georgetown, Tex.)*, **9**, 1742-1749.

26. Harmon, F.G. and Kowalczykowski, S.C. (2001) Biochemical characterization of the DNA helicase activity of the escherichia coli RecQ helicase. *J Biol Chem*, **276**, 232-243.

27. Rajagopal, V. and Patel, S.S. (2008) Single strand binding proteins increase the processivity of DNA unwinding by the hepatitis C virus helicase. *J Mol Biol*, **376**, 69-79.

28. Cadman, C.J. and McGlynn, P. (2004) PriA helicase and SSB interact physically and functionally. *Nucleic Acids Res*, **32**, 6378-6387.

29. Cui, S., Arosio, D., Doherty, K.M., Brosh, R.M., Falaschi, A. and Vindigni, A. (2004) Analysis of the unwinding activity of the dimeric RECQ1 helicase in the presence of human replication protein A. *Nucleic Acids Res*, **32**, 2158-2170.

30. Gupta, R., Sharma, S., Sommers, J.A., Kenny, M.K., Cantor, S.B. and Brosh, R.M. (2007) FANCJ (BACH1) helicase forms DNA damage inducible foci with replication protein A and interacts physically and functionally with the single-stranded DNA-binding protein. *Blood*, **110**, 2390-2398.

31. Pugh, R.A., Lin, Y., Eller, C., Leesley, H., Cann, I.K.O. and Spies, M. (2008) Ferroplasma acidarmanus RPA2 facilitates efficient unwinding of forked DNA substrates by monomers of FacXPD helicase. *J Mol Biol*, **383**, 982-998.

32. Honda, M., Park, J., Pugh, R.A., Ha, T. and Spies, M. (2009) Single-Molecule Analysis Reveals Differential Effect of ssDNA-Binding Proteins on DNA Translocation by XPD Helicase. *Mol Cell*, **35**, 694-703.

33. Qi, Z., Pugh, R.A., Spies, M. and Chemla, Y.R. (2013) Sequence-dependent base pair stepping dynamics in XPD helicase unwinding. *eLife*, **2**, e00334.

34. Ghoneim, M. and Spies, M. (2014) Direct Correlation of DNA Binding and Single Protein Domain Motion via Dual Illumination Fluorescence Microscopy. *Nano Letters*, **14**, 5920-5931.

35. Wolski, S.C., Kuper, J. and Kisker, C. (2010) The XPD helicase: XPanDing archaeal XPD structures to get a grip on human DNA repair. *Biol Chem*, **391**, 761-765.

36. Whitley, K.D., Comstock, M.J. and Chemla, Y.R. (2017) High-Resolution "Fleezers": Dual-Trap Optical Tweezers Combined with Single-Molecule Fluorescence Detection. *Methods Mol Biol*, **1486**, 183-256.

37. Kokic, G., Chernev, A., Tegunov, D., Dienemann, C., Urlaub, H. and Cramer, P. (2019) Structural basis of TFIIH activation for nucleotide excision repair. *Nature communications*, **10**, 2885.

38. Dessinges, M.N., Lionnet, T., Xi, X.G., Bensimon, D. and Croquette, V. (2004) Single-molecule assay reveals strand switching and enhanced processivity of UvrD. *Proc Natl Acad Sci U S A*, **101**, 6439-6444.

39. Comstock, M.J., Whitley, K.D., Jia, H., Sokoloski, J., Lohman, T.M., Ha, T. and Chemla, Y.R. (2015) Direct observation of structure-function relationship in a nucleic acid-processing enzyme. *Science*, **348**, 352-354.

40. Brosh, R.M., Orren, D.K., Nehlin, J.O., Ravn, P.H., Kenny, M.K., Machwe, A. and Bohr, V.a. (1999) Functional and physical interaction between WRN helicase and human replication protein A. *Journal of Biological Chemistry*, **274**, 18341-18350.

41. Brosh, R.M., Li, J.L., Kenny, M.K., Karow, J.K., Cooper, M.P., Kureekattil, R.P., Hickson, I.D. and Bohr, V.a. (2000) Replication protein A physically interacts with the Bloom's syndrome protein and stimulates its helicase activity. *J Biol Chem*, **275**, 23500-23508.

42. Doherty, K.M., Sommers, J.a., Gray, M.D., Lee, J.W., Von Kobbe, C., Thoma, N.H., Kureekattil, R.P., Kenny, M.K. and Brosh, R.M. (2005) Physical and functional mapping of the replication protein A interaction domain of the Werner and Bloom syndrome helicases. *Journal of Biological Chemistry*, **280**, 29494-29505.

43. Harami, G.M., Seol, Y., In, J., Ferencziová, V., Martina, M., Gyimesi, M., Sarlós, K., Kovács, Z.J., Nagy, N.T., Sun, Y. *et al.* (2017) Shuttling along DNA and directed processing of D-loops by RecQ helicase support quality control of homologous recombination. *Proceedings of the National Academy of Sciences*, **114**, E466-E475.

44. Pugh, R.A., Wu, C.G. and Spies, M. (2011) Regulation of translocation polarity by helicase domain 1 in SF2B helicases. *The EMBO Journal*, **31**, 503-514.

45. Arslan, S., Khafizov, R., Thomas, C.D., Chemla, Y.R. and Ha, T. (2015) Engineering of a superhelicase through conformational control. *Science*, **348**, 344-347.

46. Nguyen, B., Ordabayev, Y., Sokoloski, J.E., Weiland, E. and Lohman, T.M. (2017) Large domain movements upon UvrD dimerization and helicase activation. *Proc Natl Acad Sci U S A*, **114**, 12178-12183.

47. Comstock, M.J., Ha, T. and Chemla, Y.R. (2011) Ultrahigh-resolution optical trap with single-fluorophore sensitivity. *Nat Methods*, **8**, 335-340.

48. Berg-Sorensen, K. and Flyvbjerg, H. (2004) Power spectrum analysis for optical tweezers. *Review of Scientific Instruments*, **75**.

49. Swoboda, M., Henig, J., Cheng, H.M., Brugger, D., Haltrich, D., Plumere, N. and Schlierf, M. (2012) Enzymatic oxygen scavenging for photostability without pH drop in single-molecule experiments. *ACS Nano*, **6**, 6364-6369.

50. Landry, M.P., McCall, P.M., Qi, Z. and Chemla, Y.R. (2009) Characterization of photoactivated singlet oxygen damage in single-molecule optical trap experiments. *Biophys J*, **97**, 2128-2136.

51. Camunas-Soler, J., Ribezzi-Crivellari, M. and Ritort, F. (2016) Elastic Properties of Nucleic Acids by Single-Molecule Force Spectroscopy. *Annu Rev Biophys*, **45**, 65-84.

52. Kerssemakers, J.W., Munteanu, E.L., Laan, L., Noetzel, T.L., Janson, M.E. and Dogterom, M. (2006) Assembly dynamics of microtubules at molecular resolution. *Nature*, **442**, 709-712.